Catalysis Science & Technology

ROYAL SOCIETY OF CHEMISTRY

PAPER

View Article Online
View Journal | View Issue

Cite this: *Catal. Sci. Technol.*, 2025, **15**, 1865

Photocatalytic norfloxacin degradation enabled by a dual S-scheme nanocellulose-based Ag_2WO_4/NiO/MoO_3 tertiary heterojunction†

Shabnam Sambyal,[a] Vinay Chauhan,[a] Pooja Shandilya *[bd] and Aashish Priye*[bc]

The escalating presence of antibiotic contaminants, such as norfloxacin (NFX), in water resources poses a pressing environmental challenge, demanding the development of innovative and sustainable remediation technologies. Herein, we report the design and fabrication of a novel S-scheme heterojunction photocatalyst, comprising Ag_2WO_4, NiO, and MoO_3 nanoparticles anchored onto a nanocellulose matrix (NC–ANM), for the efficient photocatalytic degradation of NFX under visible light irradiation. Comprehensive structural, morphological, and physicochemical characterization techniques, including XRD, XPS, FTIR, FESEM, and HRTEM, corroborated the successful formation of the heterojunction and its constituent phases. Optical and electrochemical analyses, utilizing UV-vis DRS, PL, and EIS, revealed enhanced visible light absorption, efficient charge separation, and prolonged charge carrier lifetimes, key attributes underpinning the superior photocatalytic activity of the NC–ANM heterojunction. Mechanistic investigations, employing LC-MS and ESR spectroscopy, confirmed the S-scheme charge transfer pathway, leading to the generation of reactive oxygen species ($^{\bullet}OH$ and $^{\bullet}O_2^-$) that efficiently degrade NFX. The heterojunction demonstrated remarkable photocatalytic performance, achieving 99.6% NFX degradation within 30 minutes under optimized conditions. This study not only showcases the potential of NC–ANM as a highly efficient and sustainable photocatalyst for wastewater treatment but also provides valuable insights into the design and engineering of advanced S-scheme heterojunctions for environmental remediation applications.

Received 17th October 2024,
Accepted 22nd January 2025

DOI: 10.1039/d4cy01243g

rsc.li/catalysis

Introduction

In recent years, the presence of antibiotics in water sources has significantly increased.[1] Norfloxacin (NFX), a widely used synthetic fluoroquinolone antibiotic for treating human and animal diseases, is quite prominent among known contributors. Due to features like aromatic rings and heteroatoms, its chemical stability contributes to its persistence in the environment. NFX resists complete degradation, disrupting bacterial DNA replication and promoting drug-resistant bacteria. This persistence has raised concerns about reducing antibiotic residues in natural environments. Various treatment technologies have been explored, including adsorption, flocculation, and biodegradation. However, these methods face challenges such as long treatment durations, high costs, incomplete degradation, and potential secondary pollution.[2] Advanced oxidation processes (AOPs), particularly photocatalysis, have gained prominence as a sustainable and environmentally friendly solution for water purification due to their demonstrated efficacy in addressing a broad spectrum of contaminants and their inherent simplicity and mild reaction conditions.[3,4] However, individual photocatalysts have limitations such as restricted redox capability, a narrow light absorption range, and rapid recombination of photogenerated carriers, leading to reduced activity.[5,6]

To overcome the limitations of individual photocatalysts, strategies such as incorporating noble metal co-catalysts, doping, and constructing heterojunctions have been explored to enhance charge migration and broaden light absorption.[7,8] Among these, composite photocatalysts, particularly those incorporating hierarchical heterojunctions, have demonstrated significant potential for enhancing norfloxacin (NFX) degradation. Hierarchical heterojunctions, such as Z-scheme and S-scheme configurations, improve photocatalytic efficiency by facilitating effective charge separation and transfer at the

[a] *School of Advanced Chemical Sciences, Shoolini University, Solan, HP 173229, India*
[b] *Department of Chemical and Environmental Engineering, University of Cincinnati, Cincinnati, OH 45221, USA. E-mail: shandipj@ucmail.uc.edu, priyeah@ucmail.uc.edu*
[c] *Digital Futures, University of Cincinnati, Cincinnati, OH 45221, USA*
[d] *Department of Chemistry, MMEC, Maharishi Markandeshwar (Deemed to be University), Mullana-Ambala, Haryana 133207, India*
† Electronic supplementary information (ESI) available. See DOI: https://doi.org/10.1039/d4cy01243g

interfaces of semiconductors.[9] Heterojunctions broaden light absorption by utilizing distinct band gaps from different semiconductors, allowing the use of a wider range of the solar spectrum.[10] Additionally, they create an optimal environment for generating reactive superoxide and hydroxyl radicals, which are essential for effective photodegradation. The S-scheme heterojunction, a distinct configuration compared to conventional heterojunctions, further boosts photocatalytic performance by promoting selective recombination of less energetic charge carriers at the interface, thereby preserving the high redox potential of photogenerated electrons and holes.[6,11] Zhang *et al.* reported a composite photocatalyst that enhanced NFX degradation due to its optimized charge dynamics.[1] Similarly, Jin *et al.* achieved efficient degradation with N-doped TiO_2 composites, benefiting from reduced charge recombination and improved redox potential.[12] While these hierarchical heterojunctions offer advantages, challenges persist, including material cost, rapid charge recombination, and declining performance in complex environments like wastewater.

In this study, we fabricate, characterize, and harness a highly efficient S-scheme heterojunction, specifically nanocellulose-based (NC) Ag_2WO_4/NiO/MoO_3 (referred to as NC–ANM). Nanocellulose, with its tuneable surface chemistry and abundance of hydroxyl groups, serves as an ideal, sustainable substrate for constructing heterojunctions.[13,14] Nanocellulose, known for its thermal and chemical stability, combines a porous structure and high surface area with eco-friendliness and biodegradability. Its exceptional mechanical strength, transparency, and adsorption capacity make it an ideal flexible substrate for advanced optoelectronic devices. Till now, various semiconductors like metal oxides, hydrogels, carbon-based nanomaterials, nano ferrites, and perovskites have been explored.[15–20] However, here, we have focused particularly on metal oxide-based semiconductors such as Ag_2WO_4 with NiO and MoO_3 due to their superior photocatalytic properties for photodegradation application. The bare photocatalyst faced limitations such as high charge recombination, low redox ability, and poor light harnessing efficiency.

Ag_2WO_4 has a bandgap of 2.5 eV and possesses unique electronic properties.[21–25] Due to the more positive valance band (VB) position, Ag_2WO_4 exhibits strong oxidation characteristics useful in photodegradation applications. NiO, a p-type semiconductor having a bandgap of 2.16 eV, displays exceptional visible light absorption capabilities.[26–30] The more negative conduction band (CB) edge potential imparts a strong reduction ability to NiO, thereby advantageous for the generation of superoxide radicals. Similarly, MoO_3, an n-type semiconductor having a bandgap of 2.8 eV, is known for its good electron transport properties and abundance of oxygen vacancies.[31,32] Like Ag_2WO_4, the VB edges of MoO_3 also display strong oxidation potential beneficial for the generation of hydroxyl radicals. The utilization of bare photocatalysts suffers limitations such as a large bandgap, poor light absorption and photoconversion, high charge carrier recombination, poor charge migration, and leaching into the water system.

To overcome these limitations, a novel S-scheme heterojunction is prepared using Ag_2WO_4, NiO, and MoO_3 photocatalysts which are then incorporated into the nanocellulose matrix to prevent leaching and improve the stability of the photocatalysts.[33] Here, the nanocellulose acts as a support to the ANM heterojunction, providing a large surface area to efficiently adsorb and photodegrade the pollutants, and acts as an electron sink, thereby preventing the recombination of charge carriers. So far, various S-scheme-based heterojunctions have garnered significant attention, due to the unique band alignment of VB and CB edges that promote superior charge migration and prevent the recombination of highly efficient charge carriers. Further, the built-in-electric field at the interface of the S-scheme heterojunction allows the recombination of useless charge carriers which is not beneficial for photodegradation. In the S-scheme, the photocatalysts are combined in a way to either have active VB edges or CB edges for photodegradation application. For instance, the recent advancement in the 0D/2D Ag_2WO_4/WO_3 S-scheme-based heterojunction demonstrated photocatalytic performance for oxytetracycline and dye degradation due to efficient charge separation and strong oxidation capability.[24,34] Further, a bifunctional S-scheme Bi_2WO_6/NiO heterojunction demonstrates efficient ciprofloxacin degradation with enhanced carrier separation, stability, and reduced ecotoxicity of intermediates under visible light.[28,35,36] The MoO_3/g-C_3N_4 S-scheme heterojunction exhibited enhanced photocatalytic degradation of RhB under visible irradiation.[37,38] Another S-scheme heterojunction of NiFe LDH/Bi_2WO_6 achieved 75% degradation of ciprofloxacin in 60 minutes.[39] Similarly, S-scheme $ZnIn_2S_4$ nanosheets combined with cross-like FeS_2 were designed to enhance photothermal-driven H_2 evolution.[40] This S-scheme heterojunction minimized the agglomeration, increased the surface area, and established a robust interface, thereby enhancing photocatalytic activity. The advancements in S-scheme-based heterojunctions underscore the transformative potential of photocatalysts in driving efficient and sustainable photocatalytic applications. This synergistic combination of different photocatalysts with unique S-scheme charge transfer mechanisms is expected to deliver high efficiency in environmental remediation applications. ESI† Table S1 (Table S1†) presents a comprehensive overview of prior studies showcasing the efficacy of (i) nanocellulose, (ii) Ag_2WO_4, (iii) NiO, and (iv) MoO_3-based heterojunctions in achieving photodegradation.

To elucidate the structural, morphological, and chemical properties of nanocellulose, Ag_2WO_4, NiO, MoO_3, and the NC–ANM heterojunction, different techniques have been employed such as X-ray diffraction (XRD), field emission scanning electron microscopy (FESEM), high-resolution transmission electron microscopy (HRTEM), X-ray photoelectron spectroscopy (XPS), and Fourier-transform infrared spectroscopy (FTIR). UV-vis DRS, photoluminescence (PL), electrochemical impedance spectroscopy (EIS), photocurrent, and Moot Schottky analyses were also conducted to investigate the bandgap, charge recombination migration and their separation, and VB and CB

edge potentials. We then delve into a thorough investigation of the photocatalytic performance of the NC–ANM heterojunction under visible light irradiation, focusing on the degradation kinetics and efficiency of NFX removal. Additionally, we employed the electron spin resonance (ESR) spectroscopic technique and scavenging experiments to identify the key reactive oxidative species involved in NFX degradation. Finally, we have proposed the most plausible degradation pathway based on results obtained from liquid chromatography-mass spectrometry (LC-MS) analysis. The results obtained from XPS, ESR, and scavenging experiments support the formation of an S-scheme heterojunction and charge migration at the interface of the NC–ANM heterojunction.

Results and discussion

Nanocellulose was derived from pine needles through a multi-step process involving alkaline pretreatment, bleaching, and acid hydrolysis.[41] Pure Ag_2WO_4 nanorods and NiO nanoparticles were synthesized through the co-precipitation method.[42,43] MoO_3 was fabricated by a hydrothermal process followed by calcination.[44] Finally, the NC–ANM S-scheme heterojunction was formed by combining nanocellulose with Ag_2WO_4, NiO, and MoO_3 using an ultrasonic-assisted wet impregnation method, resulting in a brown-colored heterojunction (ESI;† Scheme S1).

Characterization and crystal structure

The morphology and phase composition of the as-synthesized nanomaterials were comprehensively investigated using field emission scanning electron microscopy (FESEM), high-resolution transmission electron microscopy (HRTEM), powder X-ray diffraction (PXRD), and X-ray photoelectron spectroscopy (XPS). FESEM analysis revealed an aggregated sheet-like structure for nanocellulose (Fig. 1A), consistent with the scissoring effect of H^+ ions on cellulose chains during acid hydrolysis.[45,46] Ag_2WO_4 exhibited a distinct nanorod morphology with dimensions of approximately 200 nm in length and 50 nm in width (Fig. 1B).[23] NiO nanoparticles displayed a porous structure with agglomeration of small and large particles, attributed to interparticle forces (Fig. 1C).[47] MoO_3 presented a mixed morphology of nanorods, block-like sheets, and rice-shaped particles with sizes ranging from 200–300 nm (Fig. 1D).[48] Notably, the NC–ANM heterojunction (Fig. 1E) exhibited uniform nanoparticle distribution with an average particle size distribution of 12.37 nm, attributed to the formation of nanoparticles (Fig. 1F). EDX spectra (Fig. 1G) confirmed the presence and homogeneous dispersion of C, Ni, O, Mo, Ag, and W in the NC–ANM heterojunction, corroborating the successful formation of the heterojunction. Further, HRTEM analysis confirmed the granular sheet-like, rod-like, and block-like morphologies of the individual components, with sizes ranging from 10–50 nm (ESI;† Fig. S1(a–e)). The selected area electron diffraction (SAED) pattern of NC–ANM indicates a polycrystalline nature, consistent with the uniform distribution of ANM nanoparticles on the nanocellulose surface (ESI;† Fig. S1f).

The crystallographic structures of nanocellulose, Ag_2WO_4, NiO, MoO_3, and the NC–ANM heterojunction were elucidated through XRD analysis. Nanocellulose exhibited characteristic peaks at 2θ values of 16.7°, 22.5°, and 33.9°, corresponding to the (110), (200), and (004) planes, respectively (Fig. 2A).[49,50] The absence of additional peaks confirmed the high purity of the nanocellulose, with an estimated crystallite size of 23.54 nm using the Scherrer equation. Ag_2WO_4 displayed a hexagonal phase with well-defined diffraction peaks matching 00-034-0061 (Fig. 2B), indicating a crystallite size of 30 nm. NiO exhibited a cubic phase with characteristic peaks corresponding to JCPDS#96-101-0096 (Fig. 2C),[51] and a crystallite size of 8.0 nm. MoO_3 showed a hexagonal phase with diffraction peaks matching JCPDS#21-0569 (Fig. 2D),[52] and a crystallite size of 3.0 nm. The XRD pattern of the NC–ANM heterojunction (Fig. 2E) displayed all the individual components' characteristic peaks, confirming the heterojunction's successful formation without any impurity phases. However, additional small peaks were observed in the XRD analysis of the components, indicating the presence of minor impurity phases likely arising from slight deviations in precursor stoichiometry or synthesis conditions.

The surface area and porosity of the nanomaterials and the NC–ANM heterojunction were investigated using N_2 adsorption–desorption isotherms (ESI;† Fig. S2). All the materials displayed type IV isotherms, indicative of mesoporous structures with pore diameters in the 2–50 nm range, attributed to interstitial sites within the heterojunction. As summarized in Table 1, the BET surface area and pore volume of the NC–ANM heterojunction (490 $m^2\ g^{-1}$ and 0.75 $cm^3\ g^{-1}$, respectively) were significantly higher than those of the individual components. Notably, the average pore radius for the NC–ANM heterojunction, as obtained from BET analysis, was 8.8 nm. This mesoporous structure, with a relatively narrow pore size distribution, is advantageous for photocatalytic applications as it can facilitate efficient diffusion and adsorption of pollutant molecules while providing a high density of active sites. The substantial increase in surface area and porosity of the NC–ANM heterojunction is attributed to the synergistic effect of combining nanocellulose with the metal oxide nanoparticles. The porous structure of the NC–ANM heterojunction, facilitated by the nanocellulose matrix, is expected to enhance the adsorption of reactant molecules and provide abundant active sites for photocatalytic reactions, thereby improving the overall photocatalytic efficiency of the heterojunction.

The FTIR spectrum of the NC–ANM heterojunction exhibited all the characteristic peaks of the individual components, confirming the successful formation of the heterojunction. Nanocellulose exhibited the typical O–H stretching, C–H stretching, and β-glycosidic bond vibrations.[53,54] The Ag_2WO_4 spectrum displayed prominent W–O stretching modes and characteristic W–O–W asymmetric stretching vibrations.[55] NiO exhibited the characteristic Ni–O stretching vibration, with peak

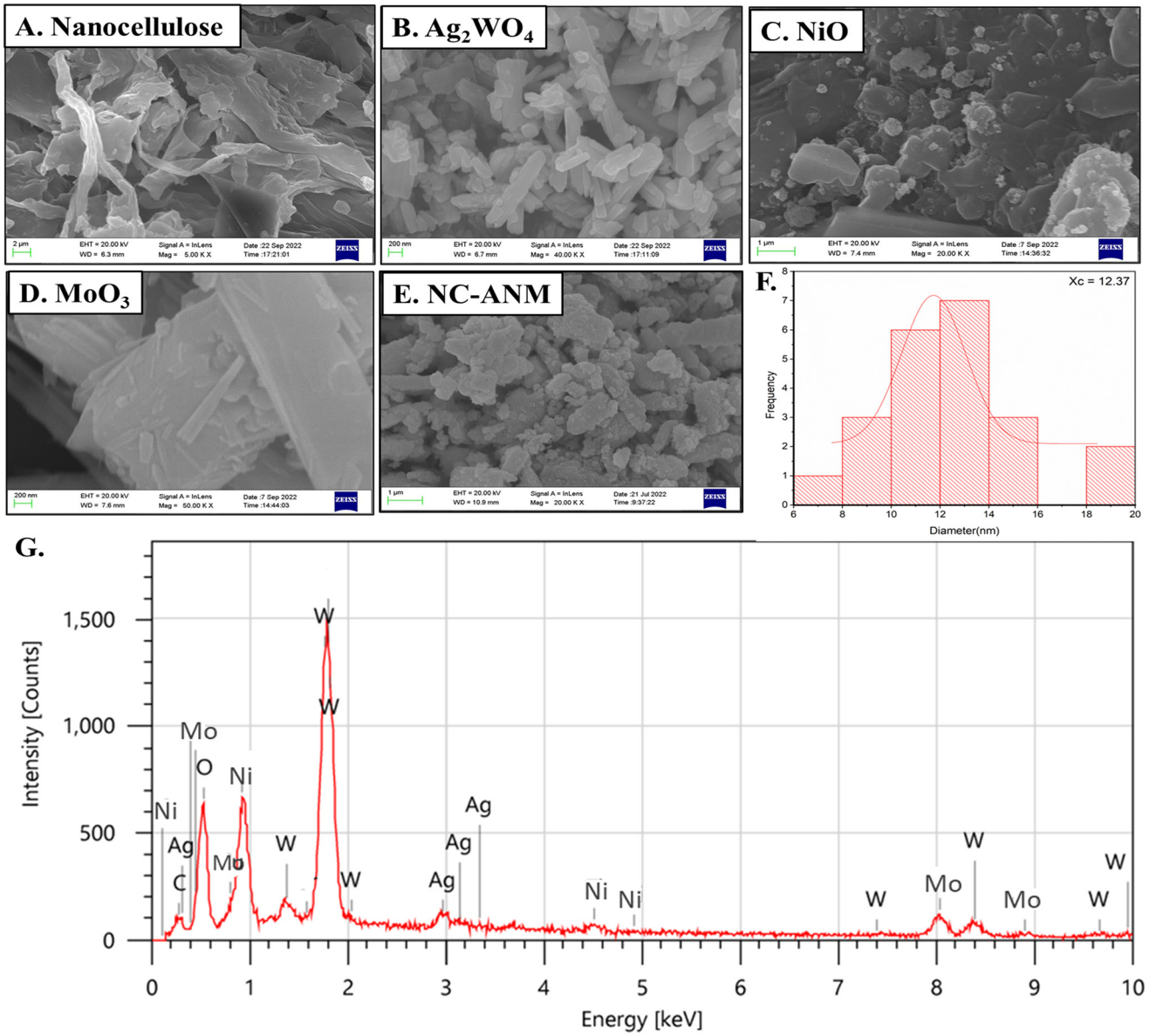

Fig. 1 Morphological and elemental characterization of the synthesized nanomaterials: FESEM images of (A) nanocellulose, (B) Ag_2WO_4, (C) NiO, (D) MoO_3, and (E) NC–ANM heterojunction, showing uniform nanoparticle distribution [scale bars = 1 μm]; (F) histogram of particle size distribution for NC–ANM, showing diameters from 8 nm to 18 nm, with an average diameter of X_c = 12.37 nm, revealing nanoparticle formation; and (G) energy-dispersive X-ray spectroscopy (EDX) spectrum of NC–ANM, showing the intensity of X-rays as a function of energy (keV). Labelled peaks correspond to characteristic X-ray emissions from elements including C, O, Ni, Mo, Ag, and W. The spectrum confirms the presence and homogeneous distribution of the constituent elements.

broadening suggesting a crystalline nature. Adsorbed CO_2 and OH groups were also observed. MoO_3 showed the distinctive terminal Mo═O double bond vibration, along with Mo–O–Mo bending and stretching modes. A slight positive shift in the typical peaks of β-glycosidic bonds and O–H bonds further indicated the successful hybridization of nanocellulose with the metal oxides[56] (ESI;† Fig. S3).

XPS analysis was conducted to elucidate the chemical composition and oxidation states of the constituent materials within the NC–ANM heterojunction (ESI;† Fig. S4). The survey scan confirmed the presence of all expected elements, including Ni, O, Ag, C, Mo, and W (Fig. 3A). High-resolution C 1s and O 1s spectra of nanocellulose (Fig. 3B and C) revealed the characteristic peaks associated with different carbon and oxygen functionalities, indicating a heterogeneous distribution of oxygen species.[57,58] For Ag_2WO_4, the Ag 3d spectrum (Fig. 3D) displayed peaks at 373.98 eV and 367.96 eV, assigned to Ag $3d_{3/2}$ and Ag $3d_{5/2}$, respectively, indicating the presence of Ag(I) and Ag(0) oxidation states.[59] These peaks shifted slightly to lower binding energies in the NC–ANM heterojunction (373.47 eV and 367.48 eV), suggesting electronic interactions between Ag_2WO_4 and the other components. Similarly, the W 4f spectrum of Ag_2WO_4 (Fig. 3E) exhibited peaks at 37.04 eV and 34.92 eV, corresponding to W $4f_{7/2}$ and W $4f_{5/2}$, respectively, confirming

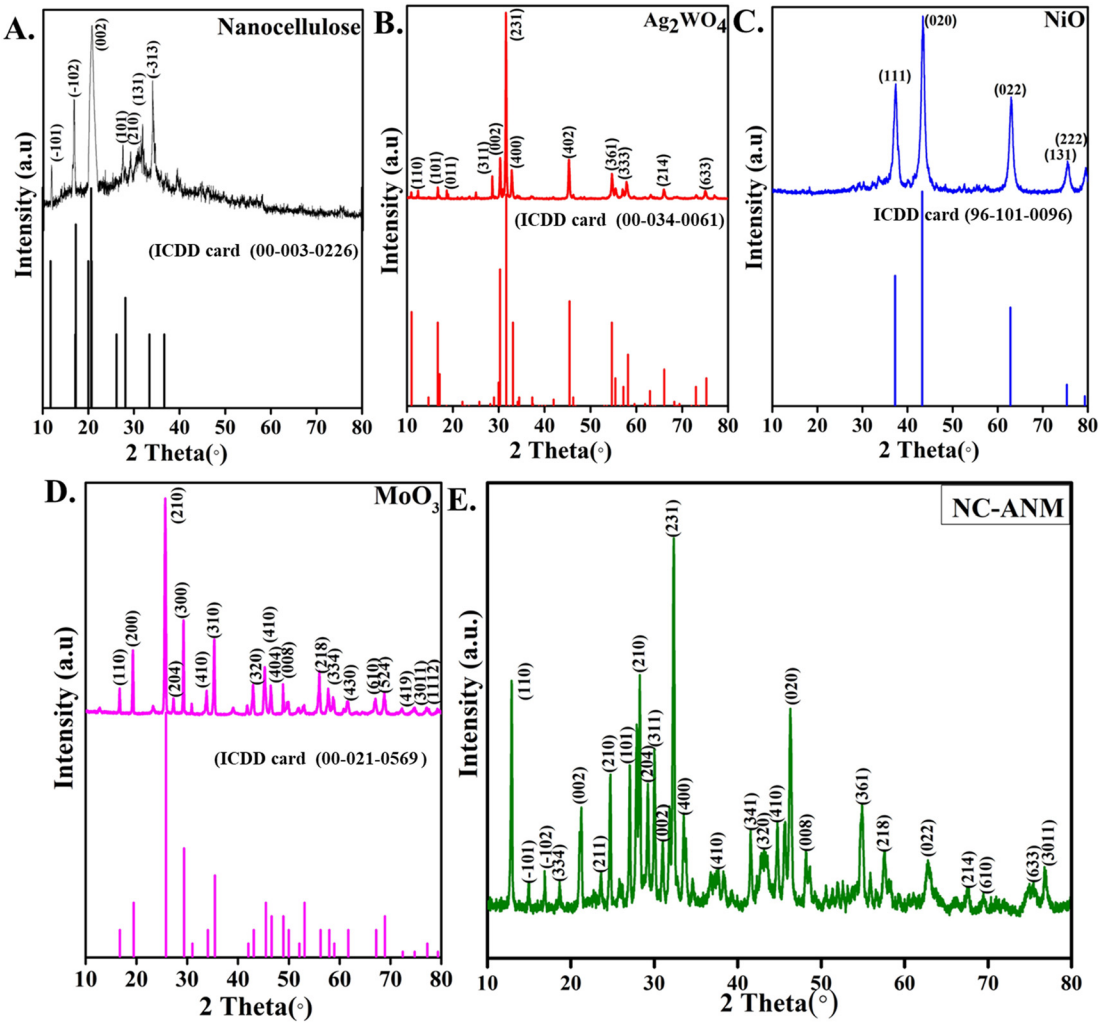

Fig. 2 XRD patterns of (A) nanocellulose, (B) Ag_2WO_4, (C) NiO, and (D) MoO_3 along with their respective ICDD references, confirming their crystallographic structures and phase purity; (E) XRD pattern of the NC–ANM heterojunction, showing the characteristic peaks of all individual components, indicative of successful heterojunction formation.

the +6 oxidation state of W.[60] These peaks also shifted slightly in the NC–ANM heterojunction (36.96 eV and 34.77 eV). The O 1s spectrum of Ag_2WO_4 (Fig. 3H) revealed two distinct peaks attributed to lattice oxygen and surface-adsorbed oxygen. Two prominent peaks for the Ni 2p orbital of NiO found at 872.64 and 855.36 eV, representing Ni $2p_{1/2}$ and Ni $2p_{3/2}$, respectively, confirmed the Ni(II) oxidation state (Fig. 3F).[46] In the NC–ANM heterojunction, these peaks were observed at slightly different binding energies (872.45 and 855.13 eV). The O 1s spectra of NiO (Fig. 3H) also showed two peaks due to lattice oxygen and surface-adsorbed oxygen. Mo 3d peaks of MoO_3 presented two peaks at 235.20 and 231.99 eV for Mo $3d_{3/2}$ and Mo $3d_{5/2}$, respectively, confirming the valence state of Mo^{6+} (Fig. 3G).[61] For NC–ANM, the Mo 3d peaks were observed at slightly different binding energies (236.03 and 232.93 eV). The O 1s spectra of MoO_3 again revealed two peaks for lattice and surface-adsorbed oxygens. These XPS results confirm the successful synthesis and composition of the NC–ANM heterojunction, with all expected chemical states and elements present.

Table 1 BET surface area and pore volume analysis of Ag_2WO_4, NiO, MoO_3, and NC–ANM heterojunction

Nanomaterial	BET surface area ($m^2\ g^{-1}$)	Pore volume ($cm^3\ g^{-1}$)
Nanocellulose	75	0.18
Ag_2WO_4	1.02	0.0045
NiO	21.56	0.09
MoO_3	15.25	0.085
NC–ANM (heterojunction)	490	0.75

To further elucidate the charge transfer mechanism within the NC–ANM heterojunction, XPS results of the constituent elements were compared between the heterojunction and the corresponding bare materials. Notably, the binding energies of Ag 3d, W 4f, and Mo 3d in the NC–ANM heterojunction exhibited negative shifts compared to their respective bare materials (Ag_2WO_4 and MoO_3), indicating increased electron

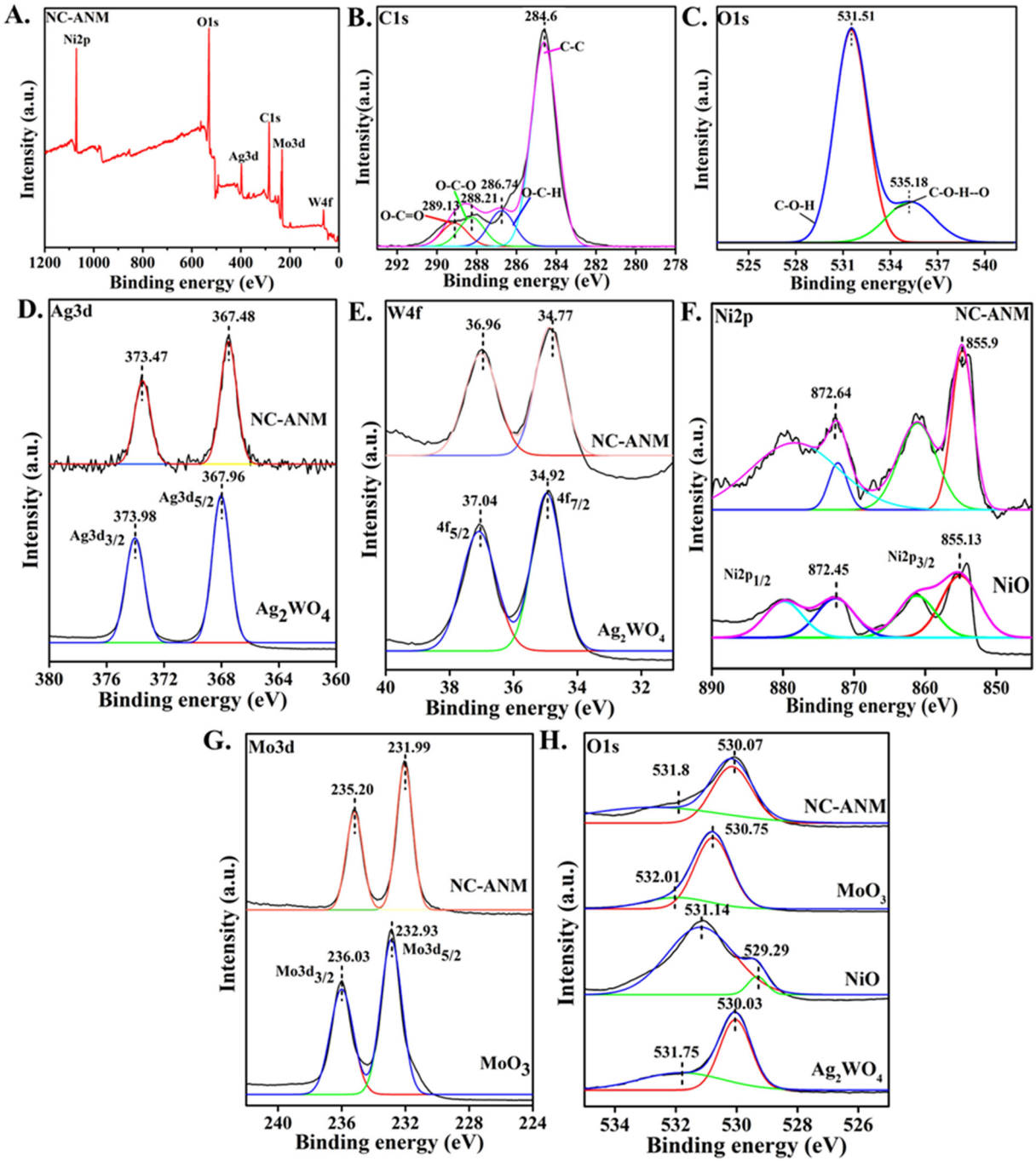

Fig. 3 XPS analysis of the NC–ANM heterojunction and its components: (A) XPS scan confirming the presence of all expected elements. High-resolution spectra of (B and C) C 1s and O 1s of nanocellulose, (D and E) Ag 3d, and W 4f of Ag_2WO_4, (F) Ni 2p of NiO, (G) Mo 3d of MoO_3, and (H) O 1s of Ag_2WO_4, NiO, and MoO_3. The observed shifts in binding energies and the presence of surface-adsorbed oxygen confirm the successful formation of the heterojunction and suggest electronic interactions between the components.

density in these components. Conversely, the binding energies of Ni 2p in NiO displayed a positive shift, suggesting decreased electron density after heterojunction formation. These shifts in binding energies strongly suggest the establishment of an internal electric field within the NC–ANM heterojunction, facilitating electron transfer from NiO to Ag_2WO_4 and MoO_3, consistent with the proposed S-scheme photocatalytic mechanism (Fig. 7D).[62]

Photoelectric performance and possible photocatalytic mechanism

The optical, electrochemical, and photoelectrochemical properties of the nanomaterials and NC–ANM heterojunction were investigated using UV-vis DRS, photoluminescence (PL), and electrochemical impedance spectroscopy (EIS). The UV-vis DRS analysis (Fig. 4A) revealed that the NC–ANM heterojunction

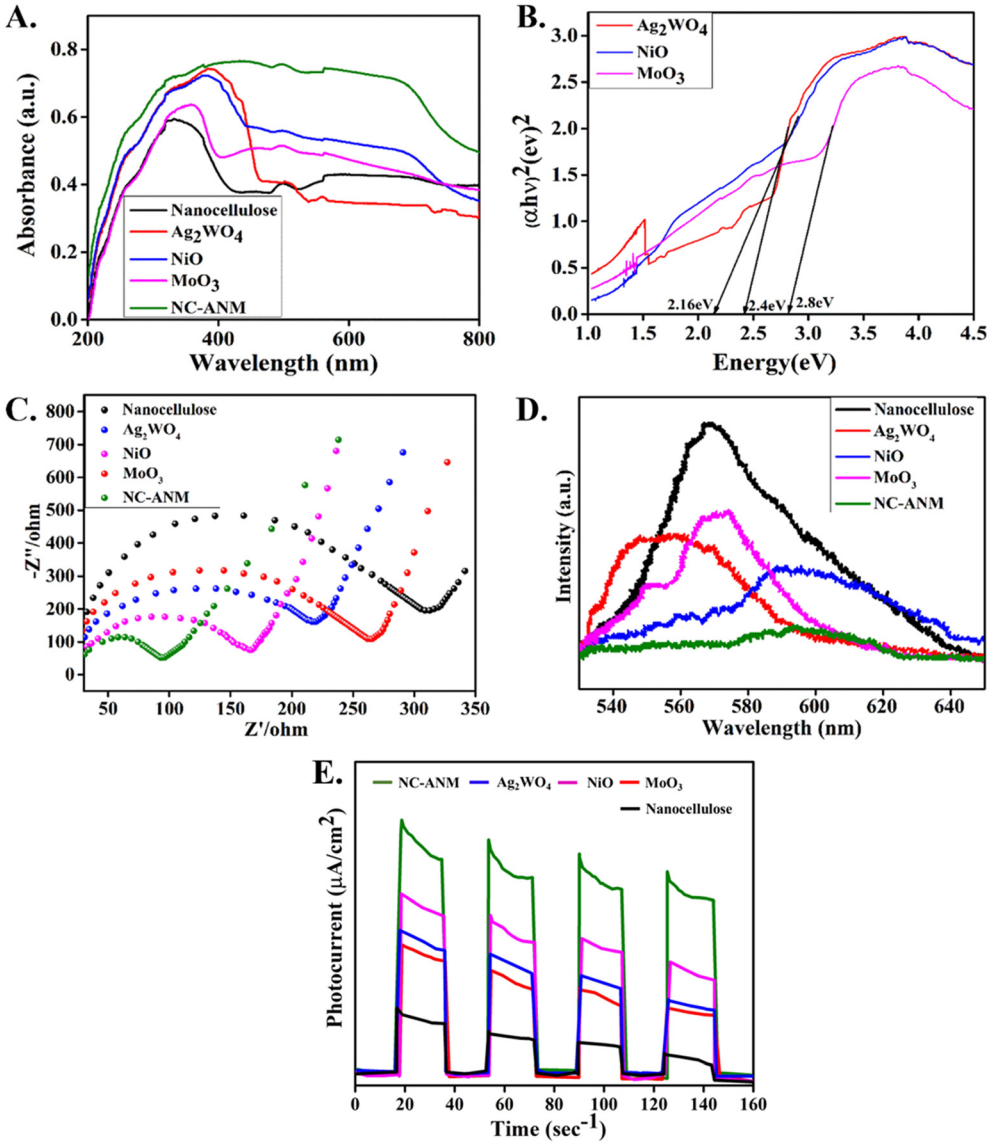

Fig. 4 (A) UV-vis diffuse reflectance spectra of nanocellulose, Ag_2WO_4, NiO, MoO_3, and NC–ANM, showing enhanced visible light absorption for the heterojunction, (B) Tauc plots for determining the band gap energies of Ag_2WO_4, NiO, and MoO_3, (C) Nyquist plots from electrochemical impedance spectroscopy, demonstrating the lower charge transfer resistance of the NC–ANM heterojunction compared to the individual components, (D) photoluminescence spectra, indicating reduced charge carrier recombination in the NC–ANM heterojunction, and (E) transient photocurrent analysis with switching cycles, where the NC–ANM heterojunction indicates high current.

exhibited a broader visible light absorption range compared to the individual components, with absorption edges at 350 nm, 392 nm, 383 nm, and 359 nm for nanocellulose, Ag_2WO_4, NiO, and MoO_3, respectively. The band gap energies of Ag_2WO_4, NiO, and MoO_3 were determined using Tauc plots (Fig. 4B; $(\alpha h\nu)^{1/n} = A(h\nu - E_g)$; h is Planck's constant, ν is the frequency, α is the absorption coefficient, A is the absorbance, and E_g is the band gap; for direct band gaps (Ag_2WO_4, NiO, MoO_3), $n = 1/2$).[63–65] Conduction band (E_{CB}) and valence band (E_{VB}) edge potentials ($E_{VB} = X - E_e + 0.5E_g$; $E_{CB} = E_{VB} - E_g$) were calculated using the electronegativity (X) of Ag_2WO_4 (5.98 eV), NiO (5.0 eV), and MoO_3 (6.37 eV), along with the free electron energy on the hydrogen scale ($E_e \approx 4.5$ eV) and band gap energies (E_g).[51–53] Calculated CB/VB values: Ag_2WO_4 (0.58/2.98 eV), NiO (1.55/−0.55 eV), and MoO_3 (3.15/0.25 eV).[66–68] The calculated CB and VB are 0.58 and 2.98 eV for Ag_2WO_4, 1.55 and −0.55 eV for NiO, and 3.15 and 0.25 eV for MoO_3, respectively.

Electrochemical impedance spectroscopy (EIS) is a powerful tool for analyzing charge transfer dynamics in photocatalytic systems.[69–72] The Nyquist plot, which depicts the imaginary impedance (Z'') against the real impedance (Z'), provides critical insights into charge transfer resistance (R_{ct}) at the electrode–electrolyte interface. A smaller semicircle in the Nyquist plot indicates a lower R_{ct}, reflecting more efficient charge separation and transfer—key factors in enhancing photocatalytic performance.[73,74] The EIS analysis (Fig. 4C) demonstrates that the NC–ANM heterojunction exhibits the smallest arc radius, corresponding to the lowest R_{ct} value among the tested

materials. The R_{ct} values, calculated as the difference between the low-frequency and high-frequency intercepts of the semicircles in the Nyquist plot, follow the trend: nanocellulose (300 Ω) > MoO_3 (270 Ω) > Ag_2WO_4 (225 Ω) > NiO (160 Ω) > NC–ANM (90 Ω). The significantly lower R_{ct} for NC–ANM indicates superior charge transfer efficiency, a result of the synergistic effects of the S-scheme heterojunction.

PL spectra (Fig. 4D) further supported this observation, as the NC–ANM heterojunction displayed reduced emission intensity compared to the individual components, suggesting a slower recombination rate of photogenerated charge carriers. This is attributed to the S-scheme charge transfer pathway within the heterojunction, which effectively separates electrons and holes, enhancing the photocatalytic efficiency.

Typically, a lower PL spectra intensity suggests reduced electron–hole recombination and a longer charge carrier life span.[75] Compared to nanocellulose, Ag_2WO_4, NiO, and MoO_3 nanocomposites, the NC–ANM heterojunction showed the weakest PL peak, indicating the most efficient separation of electrons and holes. The order of photocatalytic activity is NC <MoO_3 < NiO< Ag_2WO_4< NC–ANM. NC–ANM demonstrates enhanced activity due to its superior electron–hole separation efficiency. The transient photocurrent response is an effective method to enhance charge carrier separation and extend the lifetime of charge carriers. As shown in Fig. 4E, the highest transient photocurrent intensities are observed for nanocellulose, Ag_2WO_4, NiO, MoO_3, and the NC–ANM heterojunction. The photocurrent intensity follows the order of NC <MoO_3 < Ag_2WO_4< NiO < NC–ANM. The results displayed that the NC–ANM heterojunction exhibits excellent separation of photo-excited charge carriers due to the formation of an S-scheme heterojunction.

The position of the conduction band minimum (CBM) or valance band maximum (VBM) of the photocatalyst plays a significant role in determining its redox potential and influencing charge separation and migration at the interface.[76,77] Mott–Schottky analysis was used to investigate the flat band potential (E_{fb}) of Ag_2WO_4, NiO, and MoO_3. This involves extrapolating the linear plots to determine the following eqn (1):

$$\frac{1}{C^2} = \frac{2}{\in\in_0 q N_D}\left(E - E_{fb} - \frac{KT}{q}\right) \quad (1)$$

Here, C, q, N_D, E, E_{fb}, k, and T represent the space charge capacitance, electronic charge, donor density, applied potential, flat band potential, Boltzmann constant, and absolute temperature (in Kelvin), respectively. The figure presents the Mott Schottky plots for Ag_2WO_4, NiO, and MoO_3. The positive slopes of the linear plots confirm that Ag_2WO_4 MoO_3 and NiO are n-type and p-type semiconductors, respectively. The flat band potential values are determined to be 0.179 V(Ag_2WO_4), 0.31 (NiO), and −0.2 eV (MoO_3) referred to as Ag/AgCl. These values are calculated using the following eqn (2).

$$E_{NHE} = E_{Ag/AgCl} + 0.059 \times pH + E^{\theta}_{Ag/AgCl} \quad (2)$$

In this context, E_{NHE} represents the converted applied potential relative to the normal hydrogen electrode (NHE), and Ag/AgCl $E^{\theta}_{Ag/AgCl}$ is the standard potential of the Ag/AgCl electrode at 25 °C (0.197 V). It is accepted that the flat band potential is 0.1–0.3 V higher than the conduction band (CB) potential and lower than the valance band potential in p-type semiconductors. Consequently, the CB potential of Ag_2WO_4 and MoO_3 is 0.489 and 0.11 eV and the VB potential for NiO is 1.62 eV. Moreover, the VB potentials for Ag_2WO_4 and MoO_3 are calculated to be 2.8 and 2.94 eV, and the CB potential of NiO is −0.5 eV respectively based on their bandgaps (ESI;† Fig. S5a–d). According to the analysis, the band structure of the NC–ANM heterojunction can be formed (Fig. 7B–D). Based on the abovementioned results from the Mott–Schottky curves (Fig. S5d†), the band positions of ANM before contacts are illustrated. A potential greater than +2.24 V facilitates hydroxyl radicals, whereas a potential less than −0.33 V enables the generation of superoxide radicals. Thus, following the S-scheme heterojunction concept, Ag_2WO_4 and MoO_3 act as oxidation photocatalysts, while NiO serves as a reduction photocatalyst, respectively.

Photodegradation evaluation

The photocatalytic performance of the NC–ANM heterojunction was assessed through NFX degradation experiments in a photoreactor containing circulating water. UV-vis spectra revealed a significant decrease in NFX absorbance over time, indicating both adsorption and degradation processes (Fig. 5). The adsorption behavior of the heterojunction in the dark phase was attributed to its mesoporous nature and large surface area (490 m^2 g^{-1}) (Table 1). The pH_{pzc} of the NC–ANM heterojunction was determined to be 5.5 (ESI;† Fig. S7a), suggesting favorable adsorption of negatively charged NFX molecules at pH 6 due to electrostatic attraction.[78]

Under visible light irradiation, the NC–ANM heterojunction exhibited superior photocatalytic efficiency (99.6%) compared to the bare components (nanocellulose, Ag_2WO_4, NiO, and MoO_3) achieving nearly complete NFX degradation within 30 minutes (Fig. 5A). This enhanced performance can be attributed to the synergistic effect of the S-scheme heterojunction, facilitating efficient charge separation and transfer, as evidenced by the EIS and PL analyses. The high surface area of NC–ANM further contributed to its superior activity by providing abundant active sites for NFX adsorption and photocatalytic reactions.[79] To further evaluate the significance of the ternary heterojunction, binary composites (Ag_2WO_4/NiO, Ag_2WO_4/MoO_3, and NiO/MoO_3) were synthesized and tested under identical experimental conditions (Fig. S5a†). Among the binary composites, Ag_2WO_4/MoO_3 exhibited the highest photocatalytic efficiency. However, the NC–ANM heterojunction demonstrated significantly superior performance compared to all the binary systems, confirming the advantage of the ternary structure. The degradation efficiency followed the order: MoO_3/NiO < Ag_2WO_4/NiO < Ag_2WO_4/MoO_3 < NC–ANM.

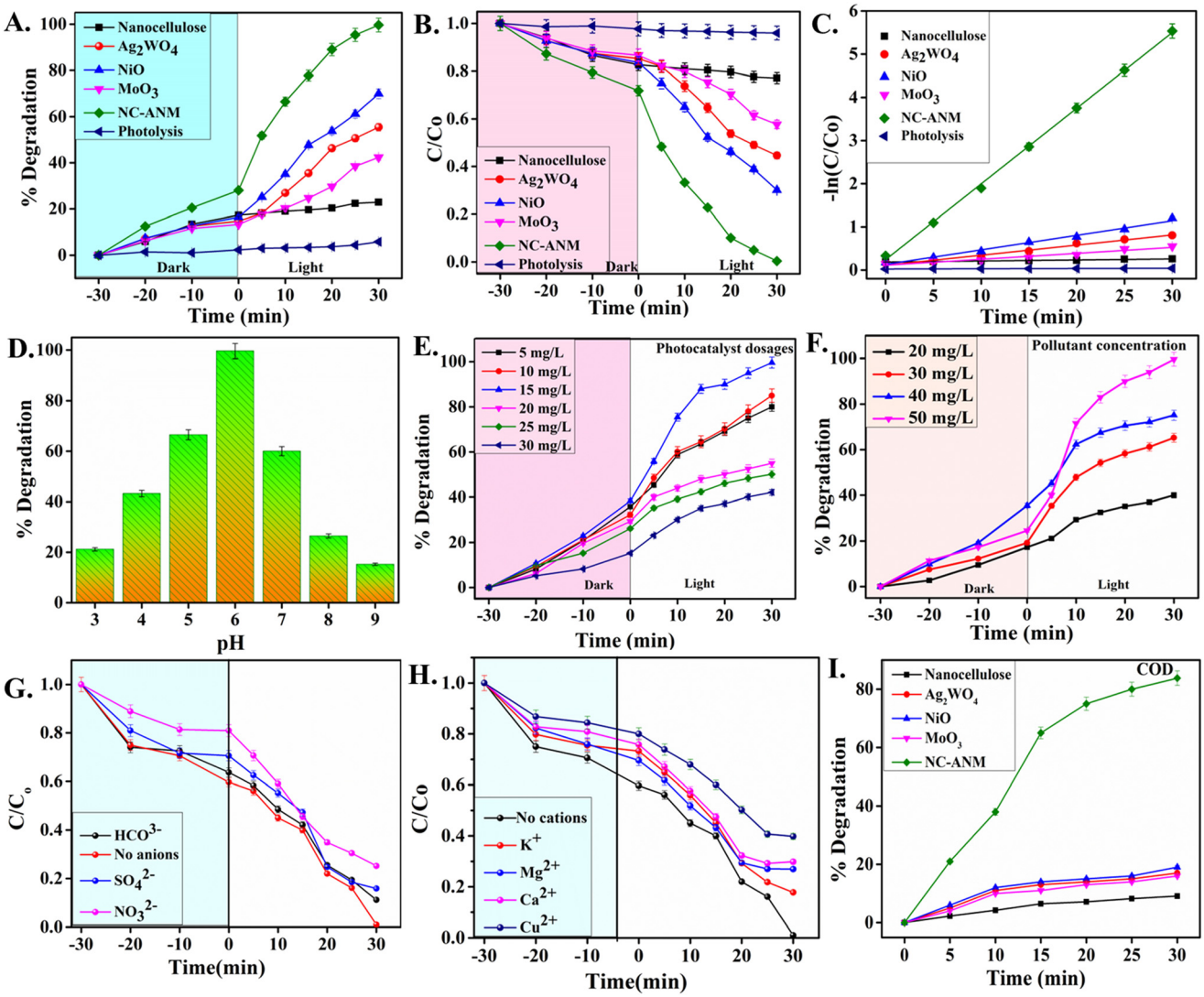

Fig. 5 The photocatalytic performance of the NC–ANM heterojunction for NFX degradation under dark and visible light conditions. (A) Percentage of degradation over time for NC–ANM and its components, showing superior performance of NC–ANM (99.6% degradation within 30 minutes), (B) and (C) kinetic analysis revealing a pseudo-first-order model with NC–ANM having the highest rate constant, (D) effect of pH on degradation efficiency (optimal pH = 6), (E) influence of photocatalyst dosage (optimal = 15 mg L^{-1}), (F) impact of initial NFX concentration on degradation, with higher concentrations slowing the reaction. The effect of common (G) anions and (H) cations in water, with HCO_3^-, SO_4^{2-}, and Cu^{2+} exhibiting inhibitory effects, and (I) chemical oxygen demand (COD) analysis demonstrating more than 80% mineralization after 30 minutes.

The kinetics of NFX photodegradation followed a pseudo-first-order model (Fig. 5B and C),[80] with NC–ANM exhibiting the highest rate constant (0.0726 h^{-1}) among the tested materials. The obtained degradation efficiency follows the order: MoO_3/NiO < Ag_2WO_4/NiO < Ag_2WO_4/MoO_3 < NC–ANM heterojunction (ESI;† Fig. S6a and b). The superior activity of NC–ANM can be attributed to the generation of hydroxyl radicals ($^{\bullet}OH$) at the active valence bands of Ag_2WO_4 and MoO_3, which play a critical role in the photodegradation process. The effects of various operational parameters, such as catalyst dosage and initial NFX concentration, on the photodegradation efficiency were investigated (Fig. 5E and F). An optimal catalyst dosage of 15 mg L^{-1} was identified for 50 mg L^{-1} NFX concentration at pH 6. The influence of pH on NFX degradation was also studied (Fig. 5D), revealing maximum efficiency at pH 6 due to the combined effects of adsorption and photocatalytic activity.

The influence of common inorganic ions on the photocatalytic degradation of NFX was evaluated to assess the feasibility of real wastewater treatment (Fig. 5G and H). Among the anions tested (NO_3^-, HCO_3^-, and SO_4^{2-}), HCO_3^- and SO_4^{2-} exhibited inhibitory effects, attributed to their scavenging of $^{\bullet}OH$ radicals, resulting in the formation of less reactive carbonate ($CO_3^{\bullet-}$) and sulfate ($SO_4^{\bullet-}$) radicals: $HCO_3^- + {}^{\bullet}OH \rightarrow CO_3^{2-} + H_2O$; $SO_4^{2-} + {}^{\bullet}OH + H^+ \rightarrow SO_4^{\bullet-} + H_2O$.

The reduced reactivity of these radicals, particularly $SO_4^{\bullet-}$, likely contributes to the observed decrease in NFX degradation rate. In contrast, NO_3^- did not show any significant inhibitory

effect. Among the cations tested (Cu^{2+}, Mg^{2+}, Ca^{2+}, and K^{+}), Cu^{2+} exhibited the most substantial inhibitory effect on NFX photodegradation. This is likely due to Cu^{2+} acting as an electron scavenger, competing with the target pollutant for photogenerated electrons and potentially occupying active sites on the catalyst surface ($Cu^{2+} + 2e^{-} \rightarrow Cu$; $Cu + 2\,h^{+} \rightarrow Cu^{2+}$).

Finally, the mineralization efficiency of NC–ANM was evaluated through chemical oxygen demand (COD) analysis (Fig. 5I). The heterojunction achieved 83.8% mineralization within 30 minutes, highlighting its effectiveness in not only degrading NFX but also mineralizing its byproducts. The inhibitory effect of Cu^{2+} was concentration-dependent, with higher concentrations leading to a more pronounced decrease in degradation efficiency. These findings highlight the importance of considering the presence of inorganic ions in real wastewater when evaluating the efficacy of photocatalytic treatment processes. Additionally, the photocatalytic efficiency of NFX degradation using various photocatalysts is reported and summarized in Table S2.† The analysis demonstrates that the NC–ANM heterojunction shows higher photocatalytic efficiency (99.6%) at a comparatively lesser time (30 min) by employing a lower (15 mg L^{-1}) photocatalyst dosage to a significantly higher (50 mg L^{-1}) NFX concentration.

The involvement of free radicals in the photocatalytic degradation process was evaluated using ESR spectroscopy with 5,5-dimethyl-1-pyrroline *N*-oxide (DMPO) as a trapping agent for $^{\bullet}OH$ and $^{\bullet}O_2^{-}$ radicals in water and methanol systems, respectively.[81,82] The NC–ANM heterojunction exhibited negligible ESR signals in the dark, indicating that both $^{\bullet}OH$ and $^{\bullet}O_2^{-}$ radicals are generated under visible light irradiation (Fig. 6A and B). The characteristic 1 : 2 : 2 : 1 intensity ESR signal

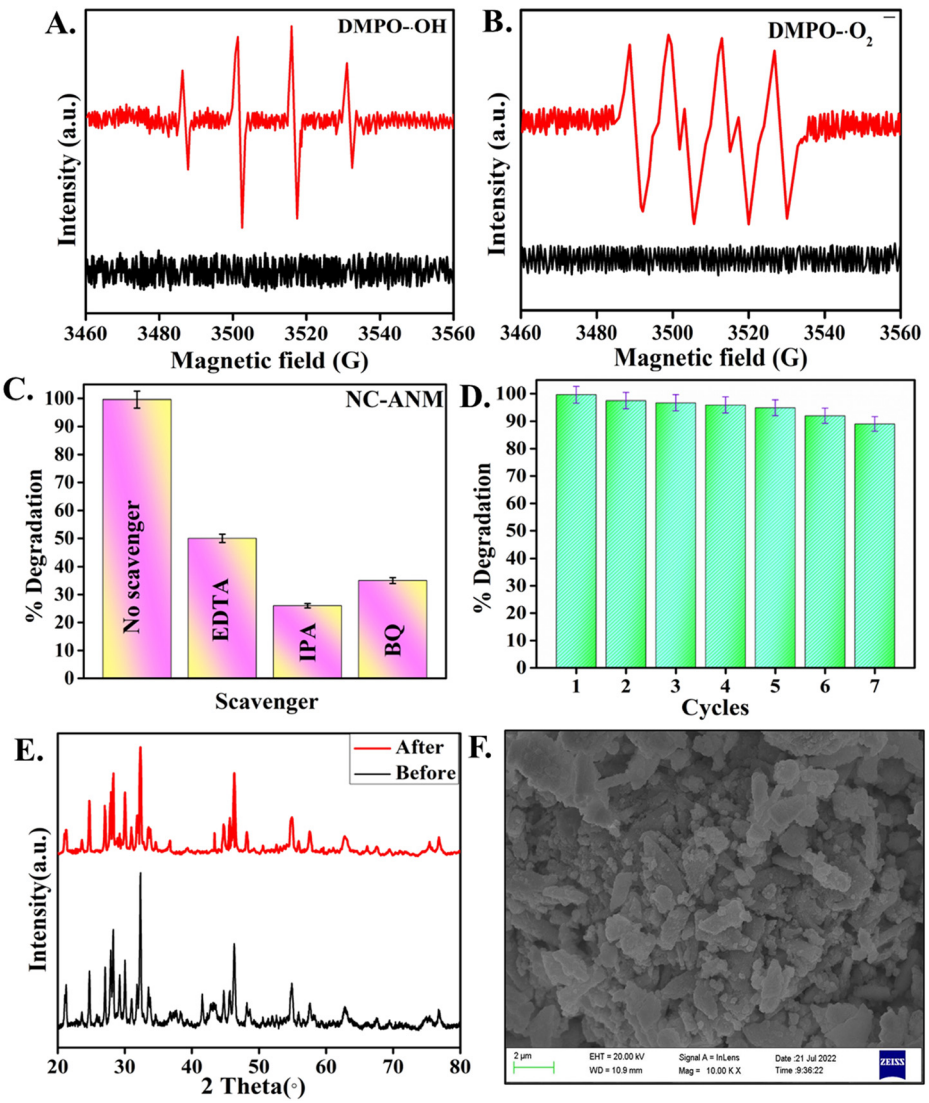

Fig. 6 ESR spectra of the NC–ANM heterojunction in the dark and under visible light irradiation, confirming the generation of (A) $^{\bullet}OH$ and (B) $^{\bullet}O_2^{-}$ radicals, (C) photocatalytic degradation of NFX in the presence of different scavengers, (D) reusability test of the NC–ANM heterojunction over seven consecutive cycles, demonstrating its excellent stability, (E) XRD and (F) FESEM analyses (scale bar = 1 μm) of the recycled NC–ANM heterojunction, showing no significant changes in surface morphology and crystal structure, respectively.

for DMPO–$^{\cdot}OH$ and DMPO–$^{\cdot}O_2^-$ adducts further confirmed the generation of these reactive species, highlighting their crucial role in the efficient photodegradation of NFX. Additionally, the ESR results support the formation of an S-scheme heterojunction in NC–ANM, as this charge transfer mechanism favors the generation of both $^{\cdot}OH$ and $^{\cdot}O_2^-$ radicals.

To further elucidate the photocatalytic mechanism, scavenging experiments were performed using IPA, BQ, and EDTA-2Na as scavengers for $^{\cdot}OH$, $^{\cdot}O_2^-$, and h^+, respectively. The addition of these scavengers significantly reduced the NFX removal efficiency from 99.6% to 25%, 46%, and 30%, respectively (Fig. 6C), underscoring the crucial roles of these reactive species in the photodegradation process.[83] For Ag_2WO_4 and MoO_3 a significant reduction in photodegradation efficiency was observed in the presence of IPA. This supports the $^{\cdot}OH$ radical as the major ROS generated at their VB and therefore both Ag_2WO_4 and MoO_3 can be labelled as oxidation photocatalysts. In contrast, their CB does not have sufficient potential to generate $^{\cdot}O_2^-$ radicals. Therefore, in the presence of BQ ($^{\cdot}O_2^-$ radical scavenger) there is no significant effect on the photodegradation efficiency of both Ag_2WO_4 and MoO_3. On the other hand, the VB of NiO (reduction photocatalysts) does not have sufficient oxidation potential to generate $^{\cdot}OH$ radicals. Meanwhile its CB can effectively generate $^{\cdot}O_2^-$ radicals, therefore, in the presence of BQ significant reduction in photodegradation efficiency is observed. Importantly, the generation of both $^{\cdot}OH$ and $^{\cdot}O_2^-$ radicals is consistent with an S-scheme charge transfer mechanism, as a type-II heterojunction would not produce these radicals on the VB of NiO and the CB of Ag_2WO_4 and MoO_3 due to their insufficient redox potentials. Trapping experiments with the individual components (Ag_2WO_4, NiO, and MoO_3) further supported this conclusion (ESI;† Fig. S7(c and d)). The presence of IPA significantly decreased the photodegradation efficiency for both Ag_2WO_4 and NiO, indicating the formation of $^{\cdot}OH$ radicals on their VB. In contrast, the addition of BQ to NiO led to a substantial reduction in efficiency, confirming the generation of $^{\cdot}O_2^-$ radicals on its CB. These findings corroborate the S-scheme charge transfer mechanism in the NC–ANM heterojunction.

The reusability of the NC–ANM photocatalyst was assessed over seven consecutive cycles. The photocatalyst maintained over 85% efficiency after the seventh cycle (Fig. 6D), demonstrating its excellent stability. FESEM and XRD analyses of the recycled material revealed no significant changes in surface morphology or crystal structure (Fig. 6E and F), further confirming its robust nature.

Possible photodegradation mechanism for NFX and S-scheme heterojunction

To elucidate the photodegradation mechanism of NFX by the NC–ANM heterojunction, LC-MS was employed to identify the intermediate products formed during the reaction. The initial presence of NFX (*m*/*z* 320) was confirmed at 0 min. Subsequent LC-MS analysis (time = 15 minutes) revealed the formation of various intermediates with different *m*/*z* values, suggesting two main degradation pathways (ESI;† Fig. S8). The first pathway involved the attack of $^{\cdot}OH$ radicals, leading to the hydroxylation of NFX and the formation of intermediates with *m*/*z* 338, 352, and 349. These intermediates corresponded to mono-, di-, and tri-hydroxylated products, respectively, with the final product also exhibiting F substitution by an $^{\cdot}OH$ group. Further degradation led to the formation of a compound with *m*/*z* 260 through the loss of H_2O molecules (Fig. 7A, pathway 1). The second pathway involved the attack of $^{\cdot}O_2^-$ ions, forming intermediates with *m*/*z* 349. The subsequent piperazine ring of NFX was first broken and then hydroformylated, and further fragmentation resulted in the formation of compounds with *m*/*z* 294, 278, and 250. The compound $C_{16}H_{16}FN_3O_5$ rapidly lost two –C═O groups to form the $C_{14}H_{16}FN_3O_3$ compound, which was hydroformylated into $C_{13}H_{11}FN_2O_4$, then lost another C═O group, forming $C_{12}H_{11}FN_2O_3$. The presence of fragments corresponding to the neutral losses of NH_3, H_2O, and CO_2 suggests the cleavage of various functional groups during the degradation process (Fig. 7A, pathway 2). These results collectively demonstrate the effective mineralization of NFX by the NC–ANM heterojunction through the generation of reactive oxygen species, primarily $^{\cdot}OH$ radicals, and the subsequent breakdown of the parent compound into smaller, less toxic intermediates. The identification of these intermediates provides valuable insights into the possible degradation pathways and highlights the potential of the NC–ANM photocatalyst for the efficient removal of NFX from contaminated water sources.

The observed shift in binding energies from XPS analysis and the efficient charge separation evidenced by ESR spectroscopy support the proposed S-scheme charge transfer mechanism in the NC–ANM heterojunction.[84,85] The difference in work functions between NiO and Ag_2WO_4/MoO_3 leads to the formation of an internal electric field at the interfaces, resulting in band bending and facilitating the recombination of less energetic charge carriers. This selective recombination process preserves highly active electrons in the CB of NiO and holes in the VB of Ag_2WO_4 and MoO_3, maximizing their redox potential. Consequently, these charge carriers can efficiently participate in redox reactions, with electrons reducing O_2 to $^{\cdot}O_2^-$ and holes oxidizing H_2O to $^{\cdot}OH$ radicals. The nanocellulose matrix further enhances the photocatalytic performance by acting as an electron trap and providing a large surface area with abundant active sites for adsorption and reaction.[54,86] The proposed mechanism, supported by trapping experiments, suggests that pollutant molecules react with photogenerated holes and $^{\cdot}OH$ radicals, while electrons in the CB of NiO contribute to $^{\cdot}O_2^-$ production. These reactive species collectively facilitate the degradation of NFX into CO_2 and H_2O (Fig. 7B–D).

Conclusion

In conclusion, we have successfully fabricated a nano cellulose-based $Ag_2WO_4/NiO/MoO_3$ S-scheme heterojunction (NC–ANM) using an ultrasonic-assisted wet impregnation

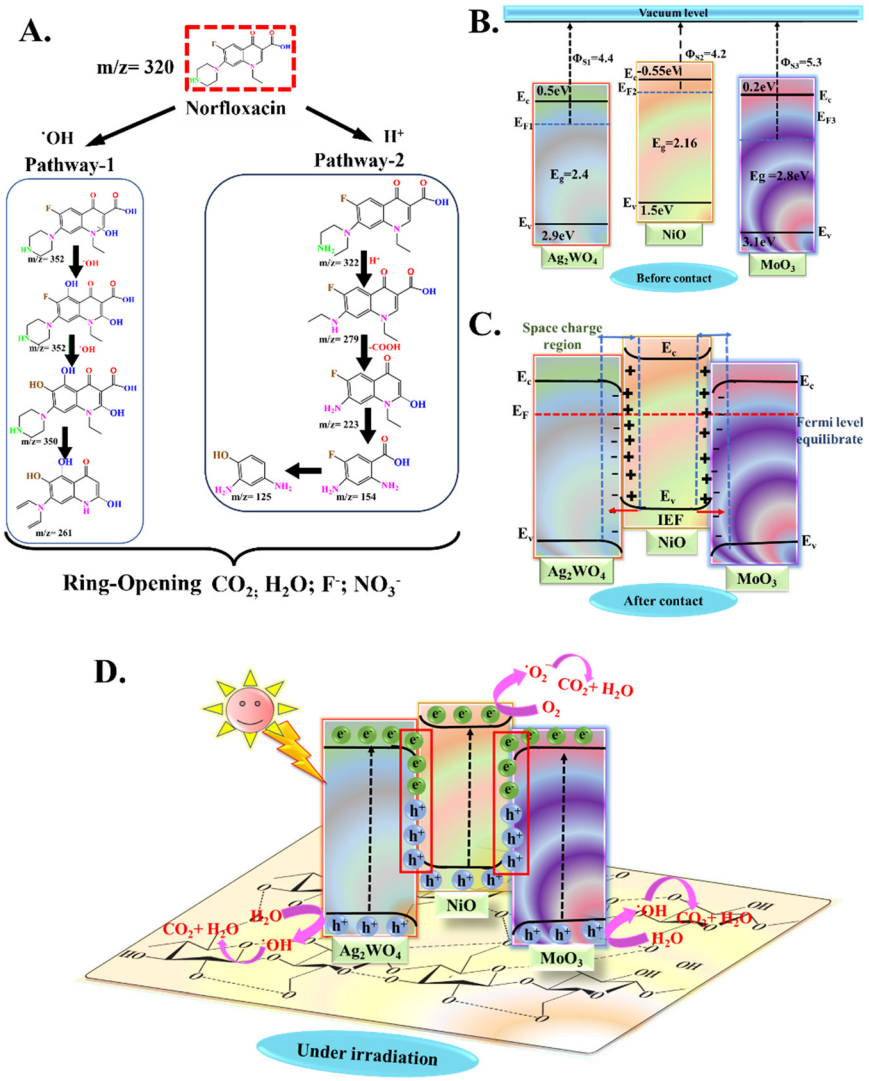

Fig. 7 (A) Proposed photodegradation pathways of NFX involving ˙OH radical attack (pathway 1) and H^+ ion attack (pathway 2); (B–D) schematic illustration of the S-scheme charge transfer mechanism in the NC–ANM heterojunction, highlighting the generation of reactive oxygen species (˙OH and $\cdot O_2^-$) and their role in NFX degradation.

approach. This novel photocatalyst exhibited a remarkable 99.6% NFX degradation efficiency within 30 minutes under optimized conditions, demonstrating significant improvement over the ANM counterpart. Comprehensive structural, optical, and electrochemical characterizations, including FESEM, HRTEM, EDS, BET, XRD, FTIR, UV-VIS DRS, PL, EIS, and photocurrent analysis, confirmed the successful formation of the heterojunction and its superior properties, such as enhanced light absorption, suppressed charge recombination, and improved charge separation. The band structure was determined by using UV-vis DRS spectroscopy and Mott–Schottky study which complemented each other. XPS and ESR spectroscopy further corroborated the establishment of the S-scheme heterojunction, enabling efficient interfacial charge transfer and the generation of reactive oxygen species (˙OH and $\cdot O_2^-$) as the primary active species for NFX degradation.

The exceptional photocatalytic performance of the NC–ANM heterojunction can be attributed to the synergistic interplay between its constituent components and the unique S-scheme charge transfer mechanism. This mechanism, driven by a stable built-in electric field and distinct band bending, facilitates the efficient separation and migration of charge carriers, maximizing their redox potential and promoting the generation of reactive oxygen species. The incorporation of nanocellulose further enhances the photocatalytic activity by providing a large surface area for adsorption and acting as an electron trap. These findings collectively demonstrate the potential of the NC–ANM S-scheme heterojunction as a highly efficient and sustainable photocatalyst for environmental remediation applications, particularly for the removal of persistent organic pollutants like NFX from wastewater. This work opens new avenues for the development of advanced photocatalytic materials that

can effectively harness solar energy for environmental protection and sustainable development.

Materials and methods

Materials

Pine needles (near the forest of Shoolini University, Solan, H. P. India), nitric acid (HNO_3,99%), sulfuric acid (H_2SO_4,99%), urea ($Co(NH_2)_2$, 98%), sodium tungstate hydrate ($Na_2WO_4.2H_2O$, 99%), sodium hydroxide (NaOH, 99%), silver nitrite ($AgNO_3$, 98%), nickel(II) nitrate hexahydrate ($NiNO_3{\cdot}6H_2O$, 98%), nickel(II) chloride ($NiCl_2$, 98%), sodium chloride ($NaClO_2$, 99.9%), ammonium molybdate ($(NH_4)_6Mo_7O_{24}$, 98%), sodium carbonate (Na_2CO_3, >99%) and norfloxacin ($C_{10}H_{18}FN_3O_3$, >98%), 1,4-benzoquinone (BQ, $C_6H_4O_2 \geq$ 98%), isopropanol (IPA, 99%), 5,5-dimethyl-1-pyrroline *N*-oxide (DMPO, 98%), ethylene diamine tetra-acetic acid (EDTA, $C_{10}H_{16}N_2O_8$ >98%), and methanol (CH_3OH, >99.8%) were procured from Sigma Aldrich. Moreover, double distilled water was utilized throughout our experiments. All chemicals are of analytic grade and were employed without necessitating further refinement.

Apparatus

The morphology of nanocellulose, Ag_2WO_4, NiO and MoO_3 was studied *via* field emission scanning electron microscopy [JSM-6100 (JEOL)] and high-resolution transmission electron microscopy (FP5022/22-Tecnai G2 20 S-TWIN) operating under 200 kV accelerating voltage. The PerkinElmer Spectrum One FTIR spectrophotometer functioning in the 4000–400 cm^{-1} range was used to detect functional groups. To determine the crystallinity of materials, PXRD (Smart Lab 9KW rotating anode X-ray diffractometer) was conducted with Cu Kα at a scan rate of 0.02° s^{-1} and 2 theta range from 10–80°. Brunauer–Emmett–Teller (Autosorb iQ3) and Barrett–Joyner–Halenda (BJH) methods at 77 K were used to determine the surface area of samples. X-ray photoelectron spectroscopy (Nexsa base) was used to observe the elemental oxidation state, chemical composition, and electron migration of photocatalysts. This analysis was also used to support the construction of the S-scheme-based heterojunction. The optical characteristics of photocatalysts were examined by using a UV-vis NIR spectrophotometer (Lambda 750 from PerkinElmer). A photoluminescence (Lab RAM HR evolution) test was conducted to assess the recombination rate of excitons in different materials. Lastly, ESR (Bruker A300–9.5/12/S/W) with temperature (100–350 K), DC-magnetic field (0–13 kg), frequency mode X band (8.75–9.65 GHz) and UV-vis irradiation (200–2000 nm wavelength) was used for electron trapping of free radicals in heterojunctions.

Photoelectrochemical evaluation

An electrochemical and photoelectrochemical investigation was undertaken using a three-electrode setup, comprising an Ag/AgCl reference electrode immersed in 3 M KCl, a Pt mesh counter electrode, and a customized fluoride-doped SnO_2 (FTO) working electrode, with 0.2 M Na_2SO_4 serving as the electrolyte. Fabrication of the working electrode involved treating a 1 cm^2 FTO substrate by immersion in acetone, followed by cleansing with ethanol and water, and subsequent plasma washing. Subsequently, 15 mg of the catalyst was dispersed in a solvent mixture comprising 10 ml of ethanol and 2 ml of triton, followed by ultrasonication for 1 hour. The resulting suspension was spin-coated onto the FTO surface to form the working electrode. Electrochemical impedance spectroscopy was conducted to assess charge migration under dark conditions. Cyclic volumetry using a Metrohm auto lab electrochemical workstation was conducted for Mott Schottky analysis by using 0.1 M sodium solution as an electrolyte. The photocurrent analysis was carried out under a 500 W Xe lamp with a three-electrode system, Ag/AgCl as a reference electrode in 3 M KCl, sample improved FTO working electrode, and Pt mesh counter electrode with 0.2 M sodium sulphate as an electrolyte.

Synthesis of materials

In the green synthesis of nanocellulose, firstly cellulose was prepared by collecting pine needles and washing them thoroughly, drying, and sieving into fine powder.[41] The suitable amount of husk underwent pretreatment using 5% NaOH solution for a duration of 3 to 4 hours in the temperature range of 80 °C while being consistently stirred. The resultant cellulose residue was filtered and washed approximately 4 to 5 times with distilled water until the wash solution became transparent and reached a neutral pH. This alkaline treatment facilitated enhanced fiber exposure for acid treatment and subsequent bleaching. The treated solution was bleached by exposure to a 5% $NaClO_2$ solution for 3 to 4 hours at 80 °C while maintaining an acidic pH. Complete removal of residual lignin was achieved through washing with distilled water. The pine needles were subsequently washed using distilled water until neutral pH was reached. The cellulose obtained was dried in an oven for 4 hours and stored for subsequent analysis and processing.

The conversion of cellulose to nanocellulose by the acid hydrolysis approach was achieved by combining 5 g of pine needle cellulose with 50 ml of 60% wt/vol H_2SO_4 acid. The mixture was then hydrolyzed at 50 °C for 80 minutes, with a continuous stirrer set at 1000 rpm. Following this, 100 ml of cold distilled water was introduced to halt the hydrolysis process. The resulting slurry was subjected to repeated washing with distilled water for about 12 minutes each time *via* centrifugation. After removing the supernatant from the sediment, the remaining residue was washed with distilled water until neutral pH was achieved using a 2% NaOH solution. Subsequently, the suspension was dispersed by ultrasonication for 12 minutes and then kept in a refrigerator at 50 °C for further utilization.

The synthesis of pure Ag_2WO_4 nanorods was conducted by the methods outlined in earlier studies using a simple co-precipitation process at room temperature without using any chemical reagent.[42] Briefly, 0.66 g of sodium tungstate was dissolved in 50 ml of deionized water and stirred for 1 hour. Similarly, 0.68 g of silver nitrate was dissolved in 50 ml of distilled water with continuous magnetic stirring for 1 hour. The later solution was then slowly added dropwise to the sodium tungstate solution and continuously mixed for 6 hours. The resulting, brown-colored suspension was thoroughly washed multiple times using ethanol and water by centrifugation. Subsequently, the final product was dried at 50 °C for further analysis and application.

NiO nanoparticles were fabricated by using a co-precipitation approach from an aqueous solution of Na_2CO_3 and an aqueous solution of $NiCl_2$.[43] Solutions of 0.25 M $NiCl_2$ and 0.5 M Na_2CO_3 were prepared in 60 ml and 120 ml of distilled water, respectively. The Na_2CO_3 solution was added drop by drop to the $NiCl_2$ solution, leading to a pH of 10. The solution was stirred for 5 hours at 50 °C, resulting in the formation of light green colored $Ni(OH)_2$ precipitates. The obtained precipitates were washed with distilled water up to neutrality (pH = 7), followed by overnight drying in an oven. Subsequently, the dried precipitates were subjected to calcination of 500 °C for 6 h.

In the fabrication of MoO_3, 5.0 g of ammonium molybdate was dissolved in 200 ml (0.5 mM) of urea with the aid of magnetic stirring for 1 hour.[44] Subsequently, the prepared solution was transferred to a Teflon-lined autoclaved and subjected to reaction for 12 hours at 180 °C. Thus, the resulting precipitate was gathered through centrifugation, washed multiple times with distilled water, and dried overnight at 100 °C. Finally, the product underwent a 3 hour calcination process at 450 °C.

Nanocomposites of nanocellulose-based metal oxide were prepared by an ultrasonic-assisted wet impregnation method by mixing equal molar concentrations of nanocellulose, Ag_2WO_4, NiO and MoO_3. The mixture was ultrasonicated for 2 h at 50 °C. After being maintained at room temperature, centrifuged and washed with distilled water several times, the NC–ANM heterojunction crystals turned brown (ESI;† Scheme S1).

Photocatalytic experiment

The photodegradation effectiveness of the as-synthesized samples was investigated for the degradation of NFX. An optimized dosage of 15 mg of photocatalyst was inserted into a 100 ml aqueous solution containing 50 mg L^{-1} of NFX. This mixture underwent constant stirring for 30 minutes to achieve adsorption–desorption equilibrium. Following this, a 50 W LED bulb was activated, and the experiment proceeded under illumination. The light source was positioned at a distance of 10–13 cm from the solution. At specific time intervals, 3 ml aliquots were withdrawn, subjected to centrifugation for 15 minutes at 3000 rpm then analyzed through absorbance studies. The concentration of NFX was quantified using UV-vis spectroscopy at 285 nm. Consequently, the photocatalyst's photodegradation efficiency was calculated using eqn (3)

$$\text{Percentage degradation efficiency} = \frac{C_0 - C_t}{C_0} \times 100 \quad (3)$$

where C_0 and C_t are the initial and final concentrations of NFX at specific time intervals, respectively.

A free radical trapping test and scavenging experiment were conducted to assess the involvement of various active free radical species in the photodegradation of NFX by NC–ANM. Hydroxyl radicals, superoxide radicals, and holes were captured using IPA, BQ, and EDTA-2Na (1 mmol L^{-1} each), respectively. By comparing the NFX photodegradation rates before and after the addition of trapping agents, we were able to identify the primary active species of NC–ANM. The recyclability tests were performed under identical conditions. After the initial experiment, the photocatalysts were extracted through centrifugation and reused for subsequent photocatalytic experiments. This process was repeated five times. To determine the optimal catalyst dosage, NFX concentration, and pH, a sequence of photodegradation experiments was conducted.

Data availability

The data underlying this study are available in the article and its online ESI.†

Conflicts of interest

There are no conflicts to declare.

Acknowledgements

This work was partially supported by the Science and Engineering Research Board, India, under the SERB International Research Experience (SIRE) Program (SIR/2022/001407). We gratefully acknowledge the support provided by the University of Cincinnati, USA.

References

1 X. Zhang, *et al.*, Construction of novel symmetric double Z-scheme BiFeO3/CuBi2O4/BaTiO3 photocatalyst with enhanced solar-light-driven photocatalytic performance for degradation of norfloxacin, *Appl. Catal., B*, 2020, **272**, 119017.
2 R. Sharma, *et al.*, Fundamentals and functional mechanisms of photocatalysis in water treatment, *Photocatalysts and Electrocatalysts in Water Remediation: From Fundamentals to Full Scale Applications*, 2022, pp. 1–37.
3 Y. Deng and R. Zhao, Advanced oxidation processes (AOPs) in wastewater treatment, *Curr. Pollut. Rep.*, 2015, **1**, 167–176.
4 D. Chen, *et al.*, Photocatalytic degradation of organic pollutants using TiO2-based photocatalysts: A review, *J. Cleaner Prod.*, 2020, **268**, 121725.

5 P. Shandilya, *et al.*, Properties, optimized morphologies, and advanced strategies for photocatalytic applications of WO3 based photocatalysts, *J. Hazard. Mater.*, 2022, **428**, 128218.
6 L. Zhang, *et al.*, Emerging S-scheme photocatalyst, *Adv. Mater.*, 2022, **34**(11), 2107668.
7 J. Xing, *et al.*, Stable isolated metal atoms as active sites for photocatalytic hydrogen evolution, *Chem. – Eur. J.*, 2014, **20**(8), 2138–2144.
8 G. Zhou, *et al.*, A general strategy via chemically covalent combination for constructing heterostructured catalysts with enhanced photocatalytic hydrogen evolution, *Chem. Commun.*, 2019, **55**(29), 4150–4153.
9 K. Li, *et al.*, MXenes as noble-metal-alternative co-catalysts in photocatalysis, *Chin. J. Catal.*, 2021, **42**(1), 3–14.
10 B. Ma, *et al.*, Molybdenum-Based Co-catalysts in Photocatalytic Hydrogen Production: Categories, Structures, and Roles, *ChemSusChem*, 2018, **11**(22), 3871–3881.
11 P. Mandyal, *et al.*, Efficient photodegradation of doxycycline and photoreduction of nitrobenzene via a dual S-scheme WO3/Cu2O/Ag3PO4 heterojunction, *Chem. Eng. J.*, 2024, **499**, 156231.
12 X. Jin, *et al.*, Photocatalytic degradation of norfloxacin using N-doped TiO2: optimization, mechanism, identification of intermediates and toxicity evaluation, *Chemosphere*, 2019, **237**, 124433.
13 P. Chawla, *et al.*, Production of nanocellulose from corn husk for the development of antimicrobial biodegradable packaging film, *Int. J. Biol. Macromol.*, 2023, **242**, 124805.
14 M. N. F. Norrrahim, *et al.*, Nanocellulose: A bioadsorbent for chemical contaminant remediation, *RSC Adv.*, 2021, **11**(13), 7347–7368.
15 P. Shandilya, *et al.*, An overview of synthesis and photocatalytic application of carbon quantum dots-based nanocomposites, *Novel Applications of Carbon Based Nanomaterials*, 2022, pp. 5–35.
16 P. Mandyal, *et al.*, A new generation of magnetic nanoferrite-based nanocomposites for environmental applications, in *Magnetic Nanoferrites and their Composites*, 2023, Elsevier, pp. 257–293.
17 P. Kumari, *et al.*, Synthesis of gum acacia-cl-acrylic acid-co-itaconic acid hydrogels for efficient removal of toxic dye rhodamine-B: A step for sustainable environment, *Int. J. Biol. Macromol.*, 2024, 139296.
18 P. Raina, *et al.*, A review on stannate perovskites-based heterojunctions and their applications in the development of sustainable technologies and materials, *Mater. Sci. Semicond. Process.*, 2025, **188**, 109224.
19 H. Yuan, *et al.*, Cobalt-based heterogeneous catalysts for photocatalytic carbon dioxide reduction, *Tungsten*, 2024, **6**(2), 410–421.
20 J. Dong, *et al.*, Highly efficient Bi/BiOCl with oxygen vacancies photocatalyst with synergetic effects of oxygen vacancy, surface plasmon resonance, and electron sink effects of metallic Bi, *Appl. Organomet. Chem.*, 2024, **38**(9), e7633.
21 Z. Chen, One-pot, room-temperature synthesis of novel Ag2WO4/AgVO3 composites with high photocatalytic activities under visible light irradiation, *J. Taiwan Inst. Chem. Eng.*, 2024, **156**, 105342.
22 Y. Sun, *et al.*, Efficient removal of lomefloxacin by Z-scheme MrGO/Ag2WO4 heterojunction recyclable composite under visible light: Mechanism of adsorption and photodegradation, *J. Environ. Chem. Eng.*, 2022, **10**(1), 107120.
23 S. Fu, *et al.*, Facile fabrication of Z-scheme Ag2WO4/BiOBr heterostructure with oxygen vacancies for improved visible-light photocatalytic performance, *J. Sci.:Adv. Mater. Devices*, 2023, **8**(2), 100561.
24 Z. H. Jabbar, *et al.*, Photocatalytic destruction of Congo red dye in wastewater using a novel Ag2WO4/Bi2S3 nanocomposite decorated g-C3N4 nanosheet as ternary S-scheme heterojunction: improving the charge transfer efficiency, *Diamond Relat. Mater.*, 2023, **133**, 109711.
25 B. Y. Balarabe, *et al.*, h-BN nanosheet-modified Ag2WO4 nanocomposite for improved photocatalytic dye removal: insights into catalyst stability and reusability, *Inorg. Chem. Commun.*, 2023, **158**, 111560.
26 T. Gul, *et al.*, Photodegradation of orange II dye using pn junction NiO/TiO2 composite, and assessment of its biological activities, *J. Saudi Chem. Soc.*, 2023, **27**(4), 101654.
27 M. Saeed, *et al.*, Synthesis of pn NiO-ZnO heterojunction for photodegradation of crystal violet dye, *Alexandria Eng. J.*, 2023, **65**, 561–574.
28 X. Hu, *et al.*, Step-scheme NiO/BiOI heterojunction photocatalyst for rhodamine photodegradation, *Appl. Surf. Sci.*, 2020, **511**, 145499.
29 J. Khan, *et al.*, Quantum-dot sensitized hierarchical NiO p–n heterojunction for effective photocatalytic performance, *RSC Adv.*, 2022, **12**(50), 32459–32470.
30 I. Ghasemi, *et al.*, Facile sono-design of 3D flower-like NiO–CuFe2O4 nano-heterostructure as an efficient and magnetically separable catalyst for photodegradation of organic dyes, *J. Cleaner Prod.*, 2022, **335**, 130355.
31 G. Harini, *et al.*, Effective photodegradation of cefixime and carvedilol mediated by visibly active MoO3/CoMn2O4/Cu2BaSnS4 photocatalytic system: An insight on photocatalytic mechanism, degradation pathway and by-product toxicity analysis, *J. Ind. Eng. Chem.*, 2024, **134**, 371–382.
32 K. Pournemati, A. Habibi-Yangjeh and A. Khataee, Rational design of TiO2/MnMoO4/MoO3 nanocomposites: Visible-light-promoted photocatalysts for decomposition of tetracycline with tandem nn heterojunctions, *Colloids Surf., A*, 2022, **655**, 130315.
33 A. F. Gouveia, *et al.*, Ag2WO4 as a multifunctional material: Fundamentals and progress of an extraordinarily versatile semiconductor, *J. Mater. Res. Technol.*, 2022, **21**, 4023–4051.
34 L. Zhou, *et al.*, Preparation of novel 0D/2D Ag2WO4/WO3 Step-scheme heterojunction with effective interfacial charges transfer for photocatalytic contaminants degradation and mechanism insight, *Chem. Eng. J.*, 2021, **420**, 130361.
35 Z. Li, *et al.*, Bi-functional S-scheme S-Bi2WO6/NiO heterojunction for photocatalytic ciprofloxacin degradation and CO2 reduction: Mechanisms and pathways, *Sep. Purif. Technol.*, 2023, **310**, 123197.

36 N. R. Reddy, *et al.*, Construction of various morphological ZnO-NiO S-scheme nanocomposites for photocatalytic dye degradation, *Inorg. Chem. Commun.*, 2022, **146**, 110107.
37 S. Swetha, *et al.*, Strategically tailored double S-scheme heterojunction in h-MoO3 doped Bi7O9I3 decorated with Cr–CdS quantum dots for efficient photocatalytic degradation of phenolics, *J. Cleaner Prod.*, 2024, **449**, 141656.
38 J. Luo, *et al.*, Excellent photocatalytic activity of MoO3-adorned g-C3N4 systems: Construction of S-scheme heterojunction, *Appl. Surf. Sci.*, 2022, **604**, 154512.
39 Q. Liu, *et al.*, Flower-like NiFe layered double hydroxide/Bi2WO6 S-scheme heterojunction for photodegradation of ciprofloxacin under visible light, *Surf. Interfaces*, 2024, **54**, 105213.
40 X. Liu, *et al.*, Anchoring ZnIn2S4 nanosheets on cross-like FeSe2 to construct photothermal-enhanced S-scheme heterojunction for photocatalytic H2 evolution, *J. Colloid Interface Sci.*, 2024, **673**, 463–474.
41 H. Onkarappa, *et al.*, Facile synthesis and characterization of nanocellulose from Zea mays husk, *Polym. Compos.*, 2020, **41**(8), 3153–3159.
42 H. J. Khadim, A. Al-Farraji and S. H. Ammar, Boosted visible-light-driven photocatalytic degradation of lomefloxacin over α-Ag2WO4/NiSx nanocomposites, *Environ. Nanotechnol., Monit. Manage.*, 2022, **18**, 100722.
43 F. Aziz, *et al.*, Facile synthesis of NiO/ZnO nano-composite by Co-precipitation, characterization and photocatalytic study of colored and colorless organic pollutants by solar irradiation, *Phys. B*, 2022, **640**, 413858.
44 S. Srinithi, V. Balakumar and S.-M. Chen, Ultra-sonic assisted synthesis of nitrogen rich-g-C3N5@ MoO3 Z-scheme system for efficient removal of acetaminophen in aqueous environment via photo-and electro-catalytically, *J. Alloys Compd.*, 2023, **957**, 170249.
45 K. Nikoofar, H. Heidari and Y. Shahedi, Nano crystalline cellulose sulfuric acid (s-NCC): a novel green nanocatalyst for the synthesis of polyhydroxy pyrimidine-fused heterocyclic compounds (PPFHs), *Cellulose*, 2018, **25**, 5697–5709.
46 E. S. A. Rashid, A. Gul, W. A. H. Yehya and N. M. Julkapli, Physico-chemical characteristics of nanocellulose at the variation of catalytic hydrolysis process, *Heliyon*, 2021, **7**(6), e07267.
47 P. Gupta, *et al.*, Effect of annealing temperature on a highly sensitive nickel oxide-based LPG sensor operated at room temperature, *Appl. Phys. A:Mater. Sci. Process.*, 2021, **127**, 1–15.
48 T. H. Chiang and H. C. Yeh, The synthesis of α-MoO3 by ethylene glycol, *Materials*, 2013, **6**(10), 4609–4625.
49 N. Pandi, S. H. Sonawane and K. A. Kishore, Synthesis of cellulose nanocrystals (CNCs) from cotton using ultrasound-assisted acid hydrolysis, *Ultrason. Sonochem.*, 2021, **70**, 105353.
50 A. Machfidho, *et al.*, Characteristics of bacterial nanocellulose composite and its application as self-cooling material, *Carbohydr. Polym. Technol. Appl.*, 2023, **6**, 100371.
51 M. Wardani, *et al.* Synthesis of NiO nanoparticles via green route using Ageratum conyzoides L. leaf extract and their catalytic activity, in *IOP Conference Series: Materials Science and Engineering*, IOP Publishing, 2019.
52 J. Solis-Vivanco, *et al.*, Optoelectrical Properties and the Study of Thickness and Annealing in Poly-3-hexylthiophene Based ITO Free Organic Solar Cells with TiO 2 and MoO 3 as Transport Layers, *Mat. Res.*, 2022, **25**, e20210416.
53 S. Zhang, *et al.*, Preparation of spherical nanocellulose from waste paper by aqueous NaOH/thiourea, *Cellulose*, 2019, **26**, 5177–5185.
54 H. Helmiyati, *et al.*, Green hybrid photocatalyst containing cellulose and γ–Fe2O3–ZrO2 heterojunction for improved visible-light driven degradation of Congo red, *Opt. Mater.*, 2022, **124**, 111982.
55 M. M. Mohamed and H. El-Farsy, Rapid reduction of nitroarenes photocatalyzed by an innovative Mn3O4/α-Ag2WO4 nanoparticles, *Sci. Rep.*, 2020, **10**(1), 21495.
56 H. Helmiyati, Y. Budiman, G. H. Abbas, F. W. Dini and M. Khalil, Highly efficient synthesis of biodiesel catalyzed by a cellulose@hematite-zirconia nanocomposite, *Heliyon*, 2021, **7**(3), e06622.
57 K. Li, *et al.*, Strong and tough cellulose nanofibrils composite films: Mechanism of synergetic effect of hydrogen bonds and ionic interactions, *ACS Sustainable Chem. Eng.*, 2019, **7**(17), 14341–14346.
58 Q. Yao, *et al.*, 3D assembly based on 2D structure of cellulose nanofibril/graphene oxide hybrid aerogel for adsorptive removal of antibiotics in water, *Sci. Rep.*, 2017, **7**(1), 1–13.
59 E. Mustafa, *et al.*, Efficient CuO/Ag 2 WO 4 photoelectrodes for photoelectrochemical water splitting using solar visible radiation, *RSC Adv.*, 2023, **13**(17), 11297–11310.
60 X. Jiang, *et al.*, Preparation and photocatalytic activity of an inorganic–organic hybrid photocatalyst Ag 2 WO 4/gC 3 N 4, *J. Inorg. Organomet. Polym. Mater.*, 2017, **27**, 1683–1693.
61 B. J. Reddy, P. Vickraman and A. S. Justin, Microwave synthesis of MoO 3-reduced graphene oxide nanocomposite for high performance asymmetric supercapacitors, *J. Mater. Sci.: Mater. Electron.*, 2019, **30**, 3618–3628.
62 B. H. Graimed, *et al.*, Rational design of 1D TaON nanofibrous network decorated 2D BiOBr nanosheets for sustainable photocatalytic detoxification of antibiotics in wastewater via S-scheme heterostructure system, *J. Water Process Eng.*, 2023, **54**, 104059.
63 M. M. Hussain, M. M. Rahman and A. M. Asiri, Ultrasensitive and selective 4-aminophenol chemical sensor development based on nickel oxide nanoparticles decorated carbon nanotube nanocomposites for green environment, *J. Environ. Sci.*, 2017, **53**, 27–38.
64 Y. Wang, Y. Kang and X. Liu, Construction of visible-light-driven ZnBi2O4/Ag2WO4 p–n heterojunction for restraining carrier recombination and improving visible-light photocatalytic performance, *J. Mater. Sci.: Mater. Electron.*, 2022, **33**(25), 19827–19838.
65 M. H. K. Neon and M. S. Islam, MoO3 and Ag co-synthesized TiO2 as a novel heterogeneous photocatalyst with enhanced visible-light-driven photocatalytic activity for methyl orange dye degradation, *Environ. Nanotechnol., Monit. Manage.*, 2019, **12**, 100244.

66 T. Munawar, *et al.*, Multi metal oxide NiO-CdO-ZnO nanocomposite–synthesis, structural, optical, electrical properties and enhanced sunlight driven photocatalytic activity, *Ceram. Int.*, 2020, **46**(2), 2421–2437.
67 A. Khan, *et al.*, Facile synthesis of a Z-scheme ZnIn2S4/MoO3 heterojunction with enhanced photocatalytic activity under visible light irradiation, *ACS Omega*, 2020, **5**(14), 8188–8199.
68 C. Mrabet, *et al.*, Structural, optical, photoluminescence and sunlight photocatalytic properties of sprayed NiO-ZnO nanocomposite thin films, *Mater. Sci. Eng., B*, 2024, **300**, 117130.
69 P. Grönroos, *et al.*, Phosphorescence and fluorescence of fibrillar cellulose films, *Nord. Pulp Pap. Res. J.*, 2018, **33**(2), 246–255.
70 S. Patnaik, G. Swain and K. Parida, Highly efficient charge transfer through a double Z-scheme mechanism by a Cu-promoted MoO 3/gC 3 N 4 hybrid nanocomposite with superior electrochemical and photocatalytic performance, *Nanoscale*, 2018, **10**(13), 5950–5964.
71 R. Alvarez-Roca, *et al.*, Selective synthesis of α-, β-, and γ-Ag2WO4 polymorphs: promising platforms for photocatalytic and antibacterial materials, *Inorg. Chem.*, 2020, **60**(2), 1062–1079.
72 M. Taeño, D. Maestre and A. Cremades, An approach to emerging optical and optoelectronic applications based on NiO micro-and nanostructures, *Nanophotonics*, 2021, **10**(7), 1785–1799.
73 Y. Zhang, *et al.*, NIR photothermal-enhanced electrocatalytic and photoelectrocatalytic hydrogen evolution by polyaniline/SnS2 nanocomposites, *ACS Appl. Nano Mater.*, 2022, **5**(1), 391–400.
74 Y. Zhang, *et al.*, Snowflake-Like Cu2S/MoS2/Pt heterostructure with near infrared photothermal-enhanced electrocatalytic and photoelectrocatalytic hydrogen production, *Appl. Catal., B*, 2022, **315**, 121540.
75 G. Zhang, *et al.*, Hydrothermal preparation of Nb5+–doped α-Fe2O3 nanorods for efficient visible light-driven photocatalytic reduction of hexavalent chromium, *Powder Technol.*, 2024, **436**, 119480.
76 Y. Li, *et al.*, Construction of self-activating Z-scheme g-C3N4/AgCl heterojunctions for enhanced photocatalytic property, *J. Phys. Chem. Solids*, 2023, **172**, 111055.
77 F. Guo, *et al.*, Facile fabrication of a CoO/gC 3 N 4 p–n heterojunction with enhanced photocatalytic activity and stability for tetracycline degradation under visible light, *Catal. Sci. Technol.*, 2017, **7**(15), 3325–3331.
78 Z. Shan, *et al.*, Kinetics and mechanism of enhanced norfloxacin degradation by Fe3O4@ La-BiFeO3 based on weak magnetization and efficient charge separation, *Chem. Eng. J.*, 2023, **466**, 143229.
79 Z. Xu, *et al.*, Enhanced photocatalytic activity by the construction of a TiO 2/carbon nitride nanosheets heterostructure with high surface area via direct interfacial assembly, *Nano Res.*, 2017, **10**, 2193–2209.
80 A. A. Mashentseva, D. T. Nurpeisova and M. Barsbay, Effect of copper doping on the photocatalytic performance of Ni 2 O 3@ PC membrane composites in norfloxacin degradation, *RSC Adv.*, 2024, **14**(7), 4424–4435.
81 M. Cai, *et al.*, A novel S-scheme heterojunction of Cd0. 5Zn0. 5S/BiOCl with oxygen defects for antibiotic norfloxacin photodegradation: performance, mechanism, and intermediates toxicity evaluation, *J. Colloid Interface Sci.*, 2023, **629**, 276–286.
82 F.-Z. Chen, *et al.*, Smart multifunctional direct Z-scheme In2S3@ PCN-224 heterojunction for simultaneous detection and photodegradation towards antibiotic pollutants, *Appl. Catal., B*, 2023, **328**, 122517.
83 J. Kang, *et al.*, Dual Z-scheme MoS2/g-C3N4/Bi24O31Cl10 ternary heterojunction photocatalysts for enhanced visible-light photodegradation of antibiotic, *J. Alloys Compd.*, 2020, **825**, 153975.
84 R. Sharma, *et al.*, Fabrication of dual S-scheme based CuWO4/NiFe/WO3 heterojunction for visible-light-induced degradation and reduction applications, *J. Environ. Chem. Eng.*, 2024, 112126.
85 P. Shandilya, A. Guleria and B. Fang, A magnetically recyclable dual step-scheme Bi2WO6/Fe2O3/WO3 heterojunction for photodegradation of bisphenol-A from aqueous solution, *J. Environ. Chem. Eng.*, 2021, **9**(6), 106461.
86 L. Lebogang, *et al.*, Ag3PO4/nanocellulose composite for effective sunlight driven photodegradation of organic dyes in wastewater, *Mater. Chem. Phys.*, 2019, **236**, 121756.